Nanoscale

ROYAL SOCIETY OF CHEMISTRY

PAPER

View Article Online
View Journal | View Issue

Cite this: *Nanoscale*, 2023, **15**, 1775

Photoresponse enhancement in a cavity–antenna-coupled graphene terahertz detector†

Jie Deng,[a,b] Jing Zhou,[a,b]* Xu Dai,[a,b] Yonghao Bu,[a,b] Zhifeng Li[a,b] and Xiaoshuang Chen*[a,b]

The unique and excellent optoelectronic properties of graphene make it a promising material for THz detection. However, the huge gap between the atomic thickness of graphene and the long wavelength of THz radiation severely limits the efficiency of light absorption and the photoresponse. Although optical antennas are commonly used to concentrate THz waves into deep subwavelength regions, a large amount of power is re-radiated out as waste rather than being absorbed by the active material. Here, we propose a cavity–antenna hybrid structure to enhance the THz absorption in a graphene flake through interference manipulation and impedance matching. The photoresponse of the device under an impedance-matched condition is 15 times higher than that under an impedance-mismatched condition. The cavity–antenna-coupled graphene THz detector exhibits a responsivity of 10.2 mA W^{-1} and a noise-equivalent power of 0.92 nW $Hz^{-0.5}$. The excellent performance of our device makes it one of the best room temperature sub-THz graphene detectors that we investigated. A theoretical model was established to analyze the interaction between the antenna-coupled graphene and the cavity structure. With a combination of both electrostatic doping and interference manipulation, the light coupling management by impedance matching can enhance the absorptance of graphene by more than two orders of magnitude. This work experimentally and theoretically revealed that the cavity–antenna hybrid structure can prominently enhance the responsivity of a tiny piece of graphene in the sub-THz regime. Meanwhile, this strategy can also be applied to enhance the absorptance of other low-dimensional or bulk materials.

Received 4th October 2022,
Accepted 18th December 2022

DOI: 10.1039/d2nr05503a

rsc.li/nanoscale

Introduction

Terahertz (THz) radiation plays an important role in the electromagnetic spectrum and attracts a lot of research interest.[1,2] THz radiation has widespread applications in various areas, such as security,[3] biomedicine,[4] imaging,[5] and communication.[6] THz detectors are the most important branch of devices for THz applications. How to efficiently convert the incoming THz power into an electrical signal becomes an essential problem. Over the past decade, the discovery of graphene has boosted the development of optoelectronic devices, including THz detectors,[7–9] due to the unique optoelectronic properties of graphene, such as high mobility, broadband absorption, low specific heat of electrons, and good compatibility with CMOS technology.[10–13] However, limited by the atomic-scale thickness and the small active area of a graphene flake, graphene-based THz detectors always suffer from insufficient THz wave coupling.[14–16] There have been numerous theoretical or simulation studies on the absorption enhancement in graphene by metamaterials,[17–20] metasurfaces,[21–23] photonic crystals,[24–26] waveguides,[27] and resonant cavities.[28–30] However, the fabrication of these complex structures still hinders the practical applications of graphene-based THz detectors. To this end, using an optical antenna to concentrate a THz wave into a graphene flake far beyond the diffraction limit is the most practical way to enhance the absorptance.[15,31] However, antennas not only receive but also radiate light power. Accordingly, they typically re-radiate out a large amount of received power as waste, and thus hinder light absorption in active materials.

In this work, we propose a cavity–antenna-coupled graphene THz detector with prominently enhanced light coupling efficiency. A cavity is simply formed by a movable metal plane at a certain distance from the antenna-coupled graphene device. Under the cavity resonance conditions, the light concentration ability of the antenna is magnified, and the light field near graphene is substantially intensified. Thus, the absorption and the responsivity are prominently enhanced. In the experiment, a 15-fold contrast in responsivity was observed

[a]*State Key Laboratory of Infrared Physics, Shanghai Institute of Technical Physics, Chinese Academy of Sciences, Shanghai 200083, China.*
E-mail: jzhou@mail.sitp.ac.cn, xschen@mail.sitp.ac.cn
[b]*University of Chinese Academy of Sciences, 19 Yuquan Road, Beijing100049, China*

† Electronic supplementary information (ESI) available. See DOI: https://doi.org/10.1039/d2nr05503a

as the cavity length changed. A maximum responsivity of 10.2 mA W^{-1} and a noise-equivalent power as low as 0.92 nW $Hz^{-0.5}$ were achieved in the cavity–antenna-coupled graphene THz detector. A theoretical model was established to analyze the interaction between the antenna-coupled graphene and the cavity. Based on the theoretical model, the absorptance of graphene shows a 40-fold difference when the Fermi level is tuned from 10 to 500 meV in simulation. This work studies the interaction between the antenna-coupled graphene and the resonant cavity structure both theoretically and experimentally, and demonstrates that the cavity structure can prominently enhance the responsivity of a tiny piece of a low-dimensional material in the THz band.

Results and discussion

The cavity–antenna-coupled graphene THz detector is shown in Fig. 1(a) and (b). The antenna-coupled graphene flake is supported by a SiO_2 (300 nm)/Si substrate (Fig. 1(c)). The bowtie antenna consists of two sectors aligned in a tip-to-tip manner. The two sectors are made from Ti/Au (15/75 nm), which serve as the source and drain contacts. The radius of each sector (L_{bowtie}) is 500 μm, and the flare angle is 60°. A piece of a mechanically exfoliated graphene flake is transferred to the feed point, where the gap is about 4 μm. The resistance of this device is 2 kΩ. According to atomic force microscopy, the graphene flake is about 5 nm thick (Fig. 1(d)). Taking the area of graphene (about 5 × 15 μm^2) into consideration, such long-wavelength light can hardly be absorbed by such a small piece of the active material.

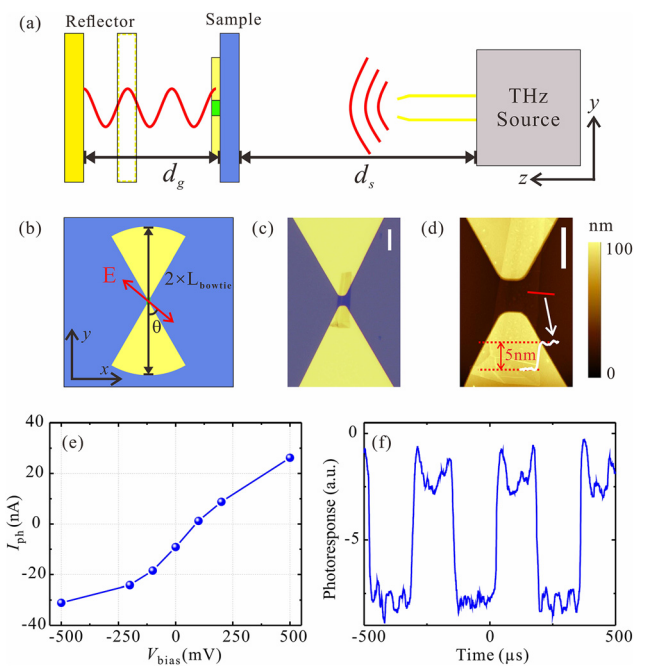

Fig. 1 (a) Schematic of the measurement setup in the y–z plane. (b) Schematic of the antenna-coupled graphene detector in the x–y plane. (c) Optical image of graphene at the center of the bowtie antenna. The scale bar is 10 μm. (c) An AFM image shows the thickness of graphene of about 5 nm. The scale bar is 5 μm. (e) The photocurrent is about 9 nA without bias and increases with the Vbias. A maximum photocurrent of 32 nA was achieved under a Vbias of −0.5 V. (f) The temporal photoresponse waveform shows a negative response.

The detector was irradiated with the THz wave from the other side of the high-resistivity silicon substrate, which is transparent to THz waves (Fig. 1(a)). The THz source emits 0.288 THz waves from a waveguide horn with polarization along the vertical direction (y-axis). The room temperature photoresponse of this device is attributed to a combination of photo-thermoelectric (PTE) and bolometric effects.[9,32–34] The zero-bias photoresponse in Fig. 1(e) mainly originates from PTE rectification, and the asymmetry between the two graphene–metal contacts is unintentionally created during the mechanical exfoliation and transfer. The non-zero-bias photoresponse is mainly attributed to the bolometric effect. Since the light-induced temperature rise causes a resistance increase in graphene, the photocurrent and the dark current have opposite polarities (Fig. 1(f)). For both photoresponse mechanisms, the responsivity is positively related to the absorptance of graphene. Thus, the key issue of enhancing responsivity is to increase the absorptance of graphene by light coupling improvement.

With the help of the bowtie antenna, the incident light is funneled into the deep subwavelength gap. However, the antenna not only receives but also radiates light, so a large portion of the power is wasted as the re-radiated wave. The incorporation of a cavity in the antenna-coupled graphene detector can manipulate the interference to reduce the re-radiation, and thus further intensify the local light field at graphene for absorption enhancement. It is interesting to note that there are actually two resonant cavities in our measurement setup (Fig. 1(a)).

The first cavity forms between the THz source and the detector. The incident THz wave is reflected by the substrate of the detector and partly transmitted to interact with the antenna-coupled graphene. The reflected wave is hardly coupled back to the horn due to the impedance mismatch. Then, it is reflected again and propagates to the sample. As the distance between the source and the detector (d_s) varies, the photocurrent of the antenna-coupled graphene detector oscillates periodically, as shown in Fig. 2(a). The period of the photocurrent oscillation is about 0.52 mm, which is just half the wavelength (λ = 1.040 mm) of the incident THz wave. This effect is attributed to the resonances of the cavity between the source and the sample. With varying d_s, the light field near the graphene periodically experiences constructive and destructive interference. Since the light confinement in the cavity between the device and the THz source is poor, the interference phenomenon is not very prominent and the maximum photocurrent is about 1.6 times higher than the minimum.

By placing a metal mirror at a distance (d_g) from the antenna-coupled graphene, a second cavity forms between the detector and the back reflector. The re-radiated wave along the positive z-axis is reflected and then interferes with the re-

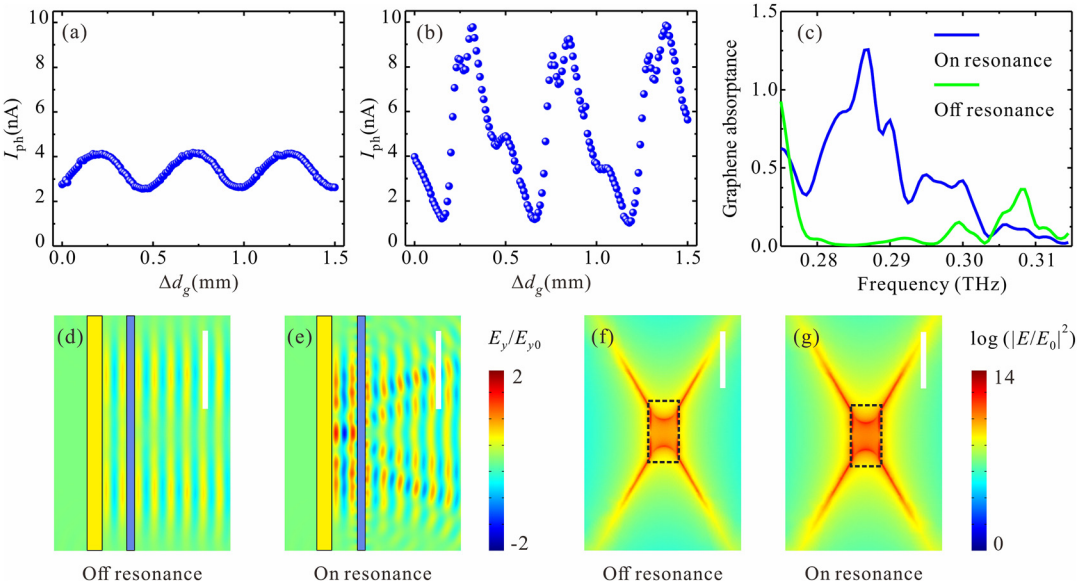

Fig. 2 (a) Photocurrent of the cavity–antenna-coupled graphene THz detector as a function of sample–source distance (d_s) without the back reflector. (b) Photocurrent as a function of air gap distance (d_g) between the sample and the reflector. (c) Simulated absorption spectra of the antenna-coupled graphene detector under on- and off-resonance conditions. (d) and (e) Simulated E_y field distributions in the y–z plane at x = 0 under the on- and off-resonance conditions, respectively. The scale bar is 5 mm. (f) and (g) Simulated localized light field (log ($|E/E_0|^2$)) near graphene under the on- and off-resonant conditions, respectively. The scale bar is 5 μm.

radiated wave in the negative z-axis. As d_g varies, the photocurrent also oscillates with a period of 0.52 mm ($\lambda/2$) as shown in Fig. 2(b). When the mirror appears at an appropriate distance from the detector, the re-radiated power is largely reduced for a specific frequency. Meanwhile, the highly localized light field near graphene (Fig. 2(g)) is expected to efficiently enhance the absorptance of graphene. In stark contrast to the first cavity, the second cavity has much better light confinement. As a result, the photocurrent under a constructive interference condition is about 15 times higher than that under a destructive interference condition (Fig. 2(b)).

The cavity structure also has an impact on the spectral response. According to the simulations (Fig. 2(c)), there is a big contrast between the on- and off-resonance graphene absorption spectra. When the metal mirror is placed at an appropriate position corresponding to the on-resonance conditions, a distinct absorption peak appears at the target detection frequency (0.288 THz) (blue solid line in Fig. 2(c)). In contrast, under the off-resonance conditions, the absorption is severely inhibited over a wide region from 0.280 THz to 0.295 THz. In the simulation, the graphene absorptance is defined as the ratio of the power absorbed by graphene to the power incident on the area of a circle circumscribing the antenna ($S_a = \pi\cdot(\lambda/2)^2$). With the help of the cavity coupled antenna, the light collection aperture could be larger than S_a. Thus, the graphene absorptance could exceed 1. Fig. 2(d) and (e) show the simulated on- and off-resonance E_y field distributions in the y–z cross section at the feed point, respectively. When the THz wave reflected by the metal plane destructively interferes with the antenna re-radiation in the negative z-axis, the re-radiation is reduced and the field at the antenna is enhanced. The antenna-coupled graphene is too small to see in Fig. 2(d) and (e). The zoom-in x–y-view light field distributions near the graphene flake under the on- and off-resonance conditions are presented in Fig. 2(f) and (g), respectively. The average light intensity over the graphene flake under the on-resonance conditions is more than 15 times higher than that under the off-resonance conditions. In addition, the light field at graphene is mainly polarized parallel to the x–y plane, and thus it can be efficiently absorbed by graphene.

To provide a deeper insight into the interesting behavior, a transmission line (TML) model was introduced for analysis. An effective surface conductivity $\sigma_{a\text{-}gr}$ was introduced to describe the antenna-coupled graphene. In the sub-THz range, it is reasonable to regard graphene as a Drude material, and the metal of the bowtie antenna as a perfect electrical conductor (PEC). As shown in Fig. 3(a) and (b), the THz wave is emitted from the source on the right-hand side. The input impedance $Z_{sub,*}$ (* = *oc* or *sc*) looking into the sample from the substrate can be expressed by:[35]

$$Z_{sub,*} = \eta_{sub}\frac{Z_{L,*} + j\eta_{sub}\tan(k_{sub}d_{sub})}{\eta_{sub} + jZ_{L,*}\tan(k_{sub}d_{sub})}(* = oc, sc) \quad (1)$$

where η_{sub} is the characteristic impedance of the substrate medium, $Z_{L,*}$ is the effective load, k_{sub} is the propagation constant in the substrate, and d_{sub} is the thickness of the substrate. The symbol * represents an open-circuit (oc) or short-circuit (sc) case, corresponding to the absence or presence of a metal reflector.

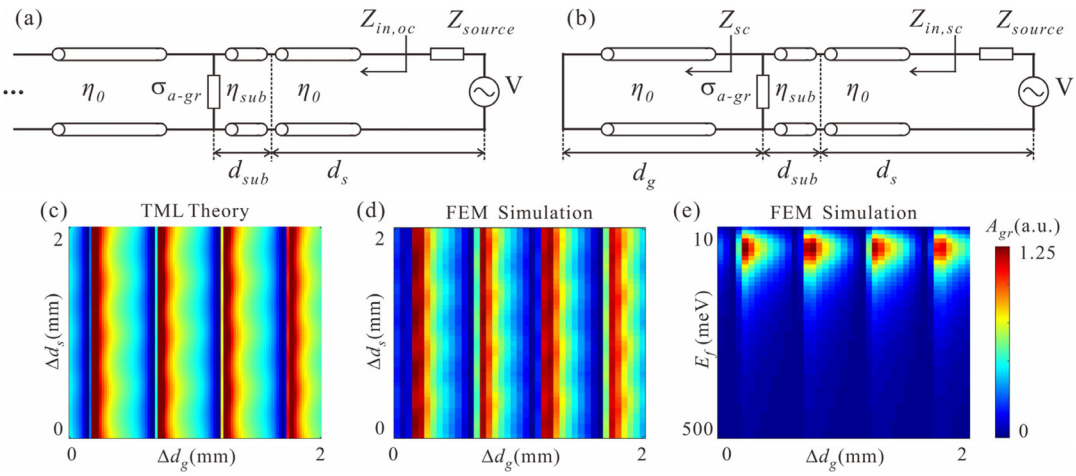

Fig. 3 (a) and (b) Transmission line models for the measurement setup. The reflector is regarded as a grounded plane, and the transmission lines of the open-circuit and short-circuit are modeled for the absence and presence of the reflector, respectively. (c) and (d) Normalization absorptance of graphene A_{gr} calculated using the TML theory and the FEM simulation as a function of Δd_s and Δd_g. (e) A_{gr} as a function of E_f and Δd_g by FEM simulation.

When the metal reflector is absent, the effective load of $Z_{L,oc}$ consists of the characteristic impedance of free space (η_0) and the impedance of the antenna-coupled graphene ($1/\sigma_{a\text{-}gr}$) in parallel (||): $Z_{L,oc} = \eta_0 \| \sigma_{a\text{-}gr}{}^{-1}$. Thus, the total input impedance $Z_{in,oc}$ looking into the sample from the source is:

$$Z_{in,oc} = \eta_0 \frac{Z_{sub,oc} + j\eta_0 \tan(k_0 d_s)}{\eta_0 + jZ_{sub,oc} \tan(k_0 d_s)} \quad (2)$$

where k_0 is the propagation constant in free space and d_s is the distance between the source and the sample. When the input impedance $Z_{in,oc}$ matches that of the source (Z_{source}), the maximum power is transferred to the load, involving a standing wave on the transmission line. Since $Z_{sub,oc}$ is fixed and $Z_{in,oc}$ varies periodically with d_s, the absorption peak periodically appears with varying d_s, and the period is equal to $\lambda/2$. The interference effect in the cavity between the sample and the source is described by the model. The photocurrent oscillating with varying d_s, as shown in Fig. 2(a), can be explained by this case. In the presence of a metal reflector, the left port changes into the short-circuited case. As the reflector moves, the length of the TML changes accordingly. The impedance of the short-circuited case, as shown in Fig. 3(b), can be regarded as a pure reactance:[36,37] $Z_{sc} = j\eta_0 \tan(k_0 d_g)$. Thus, the effective load of the short-circuit case can be written as: $Z_{L,sc} = Z_{sc} \| \sigma_{a\text{-}gr}{}^{-1}$. The total input impedance $Z_{in,sc}$ looking into the sample from the source becomes:

$$Z_{in,sc} = \eta_0 \frac{Z_{sub,sc} + j\eta_0 \tan(k_0 d_s)}{\eta_0 + jZ_{sub,sc} \tan(k_0 d_s)} \quad (3)$$

Eqn (3) can be rewritten with the auxiliary function $f(z,x,y) = x(y + jxz)/(x + jyz)$:

$$Z_{in,sc} = f(\tan(k_0 d_s), \eta_0, Z_{sub,sc})$$
$$= f(\tan(k_0 d_s), \eta_0, f(\tan(k_{sub} d_{sub}), \eta_{sub}, (j\eta_0 \tan(k_0 d_g)) \| \sigma_{a\text{-}gr}^{-1}))$$

It is clear that there are two independent variables d_s and d_g in $Z_{in,sc}$, describing the tunable dual cavities in the system. When the distance between the sample and the light source (d_s) is fixed, $Z_{in,sc}$ is a function of d_g. The light coupling efficiency changes periodically with the cavity length (d_g) due to the cavity resonances. The maximum photocurrent appears when the incident THz wave is in phase with the waves reflected by the metal plane, and the period equals $\Delta d_g = \lambda/2$ as well. The normalized absorptance of graphene A_{gr} was calculated using the TML theory. The two-dimensional diagram of A_{gr}, as a function of Δd_g and Δd_s, is shown in Fig. 3(c). Moreover, a full-wave simulation was also performed with commercial finite element method (FEM) software. The FEM simulation result (Fig. 3(d)) is consistent with the theoretical result of the TML model. Furthermore, both the FEM simulation and the TML theory calculation have good agreement with the experiment data. As shown in Fig. 3(c) and (d), when Δd_g is fixed, A_{gr} changes slightly with Δd_s. When Δd_s is fixed, A_{gr} exhibits distinct periodic variations with Δd_g. These results confirm that the dual-cavity structure could manipulate the interference and thus enhance the photoresponse of the antenna-coupled graphene THz detector. The Si substrate constitutes part of the transmission line, thus affecting phase accumulation. Nevertheless, the phase accumulation change due to the variation in d_{sub} can be compensated by adjusting the distance between the reflector and the chip (see the ESI Note 1 for details†).

Besides d_s and d_g, the effective surface conductivity $\sigma_{a\text{-}gr}$ is another parameter that influences the impedance matching. $\sigma_{a\text{-}gr}$ is determined by the antenna–graphene hybrid structure. The complex conductivity of graphene could be tuned by electrostatic gating, and the metal antenna behaves like a PEC. Fig. 3(e) plots A_{gr} as a function of the Fermi level of graphene (E_f) and Δd_g. When E_f is tuned from 10 to 500 meV, A_{gr} increases first, peaks around E_f = 50 meV, and decreases for

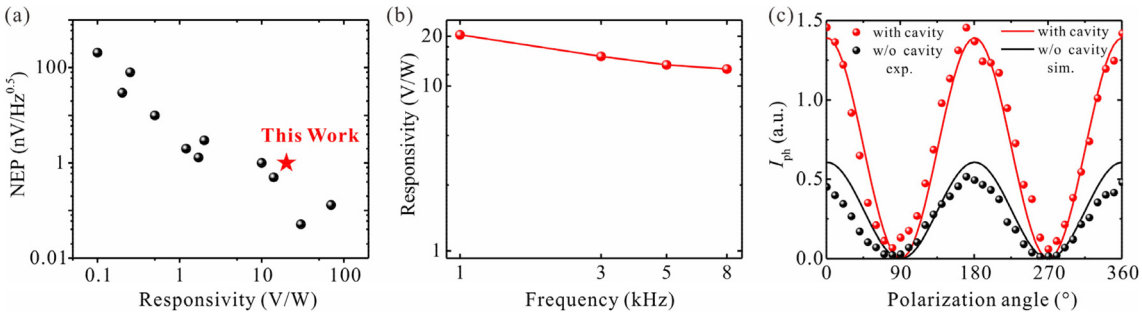

Fig. 4 (a) NEP and responsivity performances of the cavity–antenna-coupled graphene sub-THz detector and other graphene sub-THz detectors. (b) Photoresponse of the cavity–antenna-coupled graphene sub-THz detector as a function of modulation frequency. (c) Experimentally measured and FEM simulated polarization-dependent photoresponses of the antenna coupled graphene detectors with and without the cavity.

higher doping levels. The substrate of the cavity–antenna-coupled graphene THz detector is made from high-resistivity Si so that it is transparent to THz radiation. Nevertheless, the insulating substrate cannot electrostatically dope the graphene flake. In order to investigate the influence of E_f on the device performance, we prepared a new device with an extra metal back gate and a hBN flake insulating the gate from graphene. Based on the transfer characteristic measurement, the hole mobility was found to be 1400 cm^2 $(V\ s)^{-1}$ and the E_f was about 150 meV at zero gating voltage. The photoresponse reaches a peak at $E_f = 90$ meV, corresponding to the impedance matched conditions. The detailed discussion about the gating experiment can be found in the ESI Note 2.† With a combination of both electrostatic doping and interference manipulation, the light coupling management by impedance matching can enhance the absorptance of a deep subwavelength active material by more than two orders of magnitude.

Taking advantage of the cavity–antenna hybrid structure, the responsivity of our detector reached 10.2 mA W^{-1} (or 20.4 V W^{-1}) and the noise equivalent power (NEP) was calculated to be 0.92 nW $Hz^{-0.5}$. Thermal noise and shot noise are taken into account during the NEP calculation. In principle, a detector with high responsivity and low NEP is desired. A performance comparison of graphene detectors at similar sub-THz frequencies is presented in Fig. 4(a). A detectivity of 1×10^8 cm $Hz^{1/2}$ W^{-1} was calculated by $D = \sqrt{A}/\mathrm{NEP}$, where $A = S_a$ is the device active area. Our device is among the best four sub-THz graphene detectors that we investigated. The other three detectors are all based on plasma wave mixing, promoted by asymmetrical coupling between the source, drain, and gate contacts. In comparison, the high performance of our detector is due to the improved light absorption through the cavity–antenna hybrid structure, and it is compatible with various THz detectors based on different photoresponse mechanisms. Compared with several cavity-like structures, our structure has the highest light absorption enhancement ratio (see the ESI Note 3 and Table S1†).

Fig. 4(b) shows the responsivity as a function of modulation frequency. As the modulation frequency increases from 1 kHz to 8 kHz, the photoresponse slowly decreases by less than 38%, indicating that the corresponding cut-off frequency is much higher than 8 kHz. Due to the limit of the modulation speed of our THz source, the high-frequency behavior of our device was not characterized. Fig. 4(c) shows the polarization-dependent response. The antenna-coupled graphene THz detector has intrinsic polarization sensitivity. In the measurement setup, the relative polarization angle θ is defined as the angle between the polarization of the incident wave and the y-axis (Fig. 1(b)). When the polarization of the incident wave is along the y-axis, the localized THz field at the feed point is built up and the photocurrent is prominent. When the polarization is along the x-axis, the photocurrent becomes very low. As the polarization of the incident wave rotated in the x–y plane, the photocurrent was recorded as the solid circles in Fig. 4(c). The polarization dependence of the photocurrent with a resonant structure (red circles) is 3 times higher than that without the reflector (black circles). The polarization extinction ratio (PER), defined as $I_{ph}(\theta = 0°)/I_{ph}(\theta = 90°)$, is not affected by the incorporation of the cavity–antenna hybrid structure and remains about 20 for both cases. The simulation results presented by solid lines are consistent with our experiments.

Concerning the practical usage of the cavity–antenna-coupled graphene THz detector, a lens could be added in the system to focus the incident THz wave on this single pixel detector. Equipped with a TPX lens, the graphene absorptance is enhanced 11 times. The constructive interference of the THz wave in this device and the impedance matching are not affected by the focusing lens. In addition, the cavity–antenna-enhancement scheme also works for CVD-grown graphene, allowing the detectors to be wafer-scalable.[38] Although the mobility of CVD-grown graphene is much lower than that of exfoliated graphene, impedance matched conditions are also achieved by tuning the Fermi level. The optimized absorptance of CVD-grown graphene is similar to that of the exfoliated graphene. See the ESI Note 4 for details.†

Conclusions

In summary, we proposed and demonstrated a scheme of using a cavity–antenna hybrid structure to enhance the THz

light absorptance and photoresponses of a deep subwavelength graphene flake. By tuning the cavity length, the interference between the incident wave, the re-radiation, and the metal plane reflection can be manipulated to enhance the local field at graphene. When the system reaches the impedance matched conditions, the local field intensity at graphene and thus the absorptance of graphene are maximized. A 15-fold contrast in the photocurrent was observed between the impedance matched and mismatched cases. A maximum responsivity of 10.2 mA W^{-1} was achieved with a noise-equivalent power as low as 0.92 nW $Hz^{-0.5}$. According to our investigation, our cavity–antenna-coupled graphene THz detector is among the best reported room temperature graphene sub-THz detectors. A theoretical model was established to analyze the interaction between the antenna-coupled graphene and the cavity structure. Taking the tunable conductivity of graphene into consideration, the difference in absorption exceeds 40 times when the Fermi level is tuned from 10 to 500 meV in simulation. The cut-off frequency of our device is much higher than 8 kHz. The incorporation of a cavity does not affect the polarization discrimination of the detector. The polarization extinction ratio remains as high as 20. This work experimentally and theoretically revealed that the cavity resonance structure can prominently enhance the responsivity of a tiny piece of a low-dimensional material in the sub-THz regime.

Experimental section

Device fabrication

A bowtie antenna was prepared on a high-resistivity silicon substrate (ρ > 20 kΩ cm) with 300 nm SiO_2. The pattern of the planar bowtie antenna was defined by standard UV lithography, and Ti/Au (15/75 nm) electrodes were deposited by electron beam evaporation followed by a standard lift-off process. The bow radius was L_{bowtie} = 500 μm, corresponding to the strongest resonance ($2 \times L_{bowtie} = \lambda$) of around 0.288 THz (~1.040 mm). A graphene flake was prepared by mechanical exfoliation of highly oriented pyrolytic graphite (HOPG), followed by a polydimethylsiloxane (PDMS) assisted dry alignment transfer method.

Optoelectronic characterization

A commercial terahertz wave source based on IMPATT technology was used in the experiment. A millimeter-wave radiation of 0.288 THz was emitted from a horn modulated by a signal generator. To surpass the $1/f$ noise, the terahertz wave source was modulated up to 1 kHz. The back-illuminated sample was bonded to a printed circuit board (PCB) for electrical connections and then mounted in a hollow holder. The reflector was made of a silicon wafer deposited with 200 nm Au. A 5-axis stage was used for the alignment of the source, sample, and reflector. The photocurrent signal was first converted to a voltage using a low-noise current preamplifier and then detected with a lock-in amplifier or an oscilloscope. A source–drain bias voltage (V_{bias}) was applied using the preamplifier. A terahertz half-wave plate was used in polarization characterization. All measurements were carried out at room temperature and ambient pressure.

The power density of the terahertz wave source was about 357 μW cm^{-2}, calibrated using a thermal power sensor at the same position where the device was under test. The responsivity R_i was extracted from the measured I_{ph} as $R_i = I_{ph}/(P \times S_a)$, where P is the power density and S_a is the active area, defined as the area of a circle circumscribing the antenna ($S_a = \pi\cdot(\lambda/2)^2$).

The noise equivalent power (NEP) was calculated using the expression n_i/R_i, where n_i is the noise and R_i is the responsivity. Concerning the main component of the noise, the $1/f$ noise can be ruled out when the modulation frequency is higher than 300 Hz. The thermal noise n_t from the channel is the dominant noise. The shot noise n_s must be included under an external bias. Therefore, the NEP can be estimated from the following equation: $n_i^2 = n_t^2 + n_s^2 = 4kT/R_{ch} + 2qI_d$, where R_{ch} is the channel resistance and I_d is the dark current.

FEM simulation

In the THz region, the absorption of graphene is dominated by intraband transitions. The conductivity of graphene is described as:

$$\sigma_{intra} = \frac{ie^2|E_f|}{\pi\hbar^2(\omega + i\Gamma)}$$

where e is the unit of charge, $\hbar$ is the reduced Planck constant and E_f is the Fermi level, respectively. The scattering rate is described as $\Gamma = ev_f^2/\mu E_f$, where μ is the carrier mobility and v_f is the Fermi velocity.

In the FEM simulation, the metal bowtie antenna is modeled as a perfect electrical conductor (PEC) and the high-resistivity substrate is regarded as a dielectric. The carrier mobility of graphene is 2000 cm^2 $(V\ s)^{-1}$ and the tunable optical properties of graphene are achieved by varying the Fermi level E_f. The incident THz wave is emitted from a rectangle waveguide port, which is hundreds of millimeters away from the sample. To investigate the in-plane localized field near graphene, another three-dimensional simulation was carried out with the source of a Gaussian beam. Concerning the SiO_2 (300 nm)/Si substrate, SiO_2 is treated as a transparent material with a refractive index of 2.1. The high-resistivity Si is treated as a transparent material with a refractive index of 3.4.[39,40] The thickness of Si is 500 μm.

Conflicts of interest

There are no conflicts to declare.

Acknowledgements

This work was supported by the National Key Research and Development Program of China (2022YFA1404602,

2018YFA0306200); the National Natural Science Foundation of China (61975223, 91850208, 61991442 and 61874126); the Key Deployment Projects of the Chinese Academy of Sciences (ZDRW-XH-2021-7-1); the Shanghai Excellent Young Academic Leader Program (22XD1424400); the Shanghai Municipal Science and Technology Major Project (grant no. 2019SHZDZX01); and the Shanghai Tech University Quantum Device Lab (SQDL).

References

1 M. Lee and M. C. Wanke, *Science*, 2007, **316**, 64–65.
2 M. Tonouchi, *Nat. Photonics*, 2007, **1**, 97–105.
3 J. F. Federici, B. Schulkin, F. Huang, D. Gary, R. Barat, F. Oliveira and D. Zimdars, *Semicond. Sci. Technol.*, 2005, **20**, S266–S280.
4 O. A. Smolyanskaya, N. V. Chernomyrdin, A. A. Konovko, K. I. Zaytsev, I. A. Ozheredov, O. P. Cherkasova, M. M. Nazarov, J.-P. Guillet, S. A. Kozlov, Y. V. Kistenev, J.-L. Coutaz, P. Mounaix, V. L. Vaks, J.-H. Son, H. Cheon, V. P. Wallace, Y. Feldman, I. Popov, A. N. Yaroslavsky, A. P. Shkurinov and V. V. Tuchin, *Prog. Quantum Electron.*, 2018, **62**, 1–77.
5 D. M. Mittleman, *Opt. Express*, 2018, **26**, 9417–9431.
6 S. Koenig, D. Lopez-Diaz, J. Antes, F. Boes, R. Henneberger, A. Leuther, A. Tessmann, R. Schmogrow, D. Hillerkuss, R. Palmer, T. Zwick, C. Koos, W. Freude, O. Ambacher, J. Leuthold and I. Kallfass, *Nat. Photonics*, 2013, **7**, 977–981.
7 T. Low and P. Avouris, *ACS Nano*, 2014, **8**, 1086–1101.
8 J. Yang, H. Qin and K. Zhang, *Opt. Commun.*, 2018, **406**, 36–43.
9 J. Liu, X. Li, R. Jiang, K. Yang, J. Zhao, S. A. Khan, J. He, P. Liu, J. Zhu and B. Zeng, *Sensors*, 2021, **21**, 4987.
10 C. J. Docherty and M. B. Johnston, *J. Infrared Millimeter, Terahertz Waves*, 2012, **33**, 797–815.
11 L. Vicarelli, M. S. Vitiello, D. Coquillat, A. Lombardo, A. C. Ferrari, W. Knap, M. Polini, V. Pellegrini and A. Tredicucci, *Nat. Mater.*, 2012, **11**, 865–871.
12 F. H. L. Koppens, T. Mueller, P. Avouris, A. C. Ferrari, M. S. Vitiello and M. Polini, *Nat. Nanotechnol.*, 2014, **9**, 780–793.
13 A. Rogalski, *Adv. Opt. Photonics.*, 2019, **11**, 314.
14 Y. Li, K. Tantiwanichapan, A. K. Swan and R. Paiella, *Nanophotonics*, 2020, **9**, 1901–1920.
15 Q. Li, J. Lu, P. Gupta and M. Qiu, *Adv. Opt. Mater.*, 2019, **7**, 1900595.
16 Y. Li, Y. Zhang, Y. Yu, Z. Chen, Q. Li, T. Li, J. Li, H. Zhao, Q. Sheng, F. Yan, Z. Ge, Y. Ren, Y. Chen and J. Yao, *Photonics Res.*, 2020, **8**, 368–374.
17 Y. Zhang, Y. Feng, B. Zhu, J. Zhao and T. Jiang, *Opt. Express*, 2014, **22**, 22743–22752.
18 L. Ye, Y. Chen, G. Cai, N. Liu, J. Zhu, Z. Song and Q. H. Liu, *Opt. Express*, 2017, **25**, 11223–11232.
19 G. Deng, P. Chen, J. Yang, Z. Yin and L. Qiu, *Opt. Commun.*, 2016, **380**, 101–107.
20 P.-Y. Chen and A. Alu, *IEEE Trans. Terahertz Sci. Technol.*, 2013, **3**, 748–756.
21 L. Ye, X. Chen, G. Cai, J. Zhu, N. Liu and Q. H. Liu, *Nanomaterials*, 2018, **8**, 562.
22 Y. Deng, L. Peng, X. Liao and X. Jiang, *Plasmonics*, 2019, **14**, 1057–1061.
23 S. Guo, J. Deng, J. Zhou, Y. Yu, Y. Bu, T. Zhu, X. Ren, Z. Li, W. Lu and X. Chen, *Opt. Express*, 2021, **29**, 9269.
24 J. R. Piper and S. Fan, *ACS Photonics*, 2014, **1**, 347–353.
25 J. R. Piper, V. Liu and S. Fan, *Appl. Phys. Lett.*, 2014, **104**, 251110.
26 Y. Fan, L. Tu, F. Zhang, Q. Fu, Z. Zhang, Z. Wei and H. Li, *Plasmonics*, 2018, **13**, 1153–1158.
27 N. Joshi and N. P. Pathak, *Plasmonics*, 2017, **12**, 1545–1554.
28 B. Vasić and R. Gajić, *Opt. Lett.*, 2014, **39**, 6253.
29 L. Jiang, J. Guo, L. Wu, X. Dai and Y. Xiang, *Opt. Express*, 2015, **23**, 31181–31191.
30 J. Min Woo, M.-S. Kim, H. Woong Kim and J.-H. Jang, *Appl. Phys. Lett.*, 2014, **104**, 081106.
31 V. Giannini, A. I. Fernández-Domínguez, S. C. Heck and S. A. Maier, *Chem. Rev.*, 2011, **111**, 3888–3912.
32 J. C. W. Song, M. S. Rudner, C. M. Marcus and L. S. Levitov, *Nano Lett.*, 2011, **11**, 4688–4692.
33 R.-B. Tan, H. Qin, J.-D. Sun, X.-Y. Zhang and B.-S. Zhang, *Appl. Phys. Lett.*, 2013, **103**, 173507.
34 A. V. Muraviev, S. L. Rumyantsev, G. Liu, A. A. Balandin, W. Knap and M. S. Shur, *Appl. Phys. Lett.*, 2013, **103**, 181114.
35 A. Andryieuski and A. V. Lavrinenko, *Opt. Express*, 2013, **21**, 9144.
36 M. Liu, Q. Yang, A. A. Rifat, V. Raj, A. Komar, J. Han, M. Rahmani, H. T. Hattori, D. Neshev, D. A. Powell and I. V. Shadrivov, *Adv. Opt. Mater.*, 2019, **7**, 1900736.
37 Y. Ra'di, A. Krasnok and A. Alù, *ACS Photonics*, 2020, **7**, 1468–1475.
38 M. Asgari, E. Riccardi, O. Balci, D. De Fazio, S. M. Shinde, J. Zhang, S. Mignuzzi, F. H. L. Koppens, A. C. Ferrari, L. Viti and M. S. Vitiello, *ACS Nano*, 2021, **15**, 17966–17976.
39 R. Kitamura, L. Pilon and M. Jonasz, *Appl. Opt.*, 2007, **46**, 8118.
40 F. Sanjuan and J. O. Tocho, in *Latin America Optics and Photonics Conference*, OSA, Sao Sebastiao, 2012, p. LT4C.1.